

# Reconstruction of Atomic Ionization Probabilities in Intense Laser Fields

T R J Goodworth<sup>1</sup>, W A Bryan<sup>1</sup>, I D Williams<sup>2</sup>  
and W R Newell<sup>1</sup>

1) Department of Physics and Astronomy, University College London, Gower Street, London WC1E 6BT, UK

2) Department of Physics, Queen's University Belfast, Belfast BT7 1NN, UK

**Abstract.** Application of a parallel-projection inversion technique to z-scan spectra of multiply charged xenon and krypton ions, obtained by non-resonant field ionization of neutral targets, has for the first time permitted the direct observation of intensity-dependent ionization probabilities. These ionization efficiency curves have highlighted the presence of structure in the tunnelling regime, previously unobserved under full-volume techniques.

## 1. Introduction

Multiple atomic ionization within intense ( $> 10^{14} \text{ Wcm}^{-2}$ ) non-resonant laser fields is an area of considerable interest [1] involving non-linear phenomena such as above-threshold ionization, non-sequential ionization [2], and high harmonic generation [3]. Early investigations collected ion signal from the full confocal volume, see for example [4]. As such, detected ion yields represented a convolution of all active intensity-dependent ionization processes. The use of a full confocal volume also meant that the ion yield curves as a function of peak laser intensity followed the characteristic  $I^{3/2}$  behaviour within the saturated field ionization regime. The first attempt to limit this gross spatial integration used a pinhole aperture to image the centre of a shallow laser focus [5]. Under this configuration intensity variation was achieved by conventional half-wave plate energy attenuation techniques. The generalised dependence of total ionization has also been studied by soft focusing the laser beam into an approximately cylindrical configuration as viewed by the ion detector [6]. More recently, intensity selective scanning has been successfully implemented through z-scanning [7, 8]. This technique uses a slit of width  $\Delta z$  to limit the detected intensity range along the laser propagation ( $z$ ) axis, in this case the intensity variation is accessed by translating the laser focus along the laser propagation ( $z$ ) axis with respect to the masking aperture using the natural, on-axis (Lorentzian) intensity variation  $I_z = I_0/(1 + (z/z_o)^2)$ , where  $z_o = \pi\omega_0^2/\lambda$  is the Rayleigh range. This technique also has the advantage that lower intensity processes are accessed with increased interaction volumes due to the shape of the confocal volume, see for example [9]. Despite the quantisation of the intensity variation along the  $z$ -axis with this technique, the radial intensity variation remains unbound. As such, the powerful  $z$ -scan technique is restricted to the determination of threshold ( $I_{th}$ ) and saturation ( $I_{sat}$ ) intensities by Gaussian volume fitting [8]. Clearly, if the radial intensity variation were quantised in a similar way to the  $z$ -axial variation,

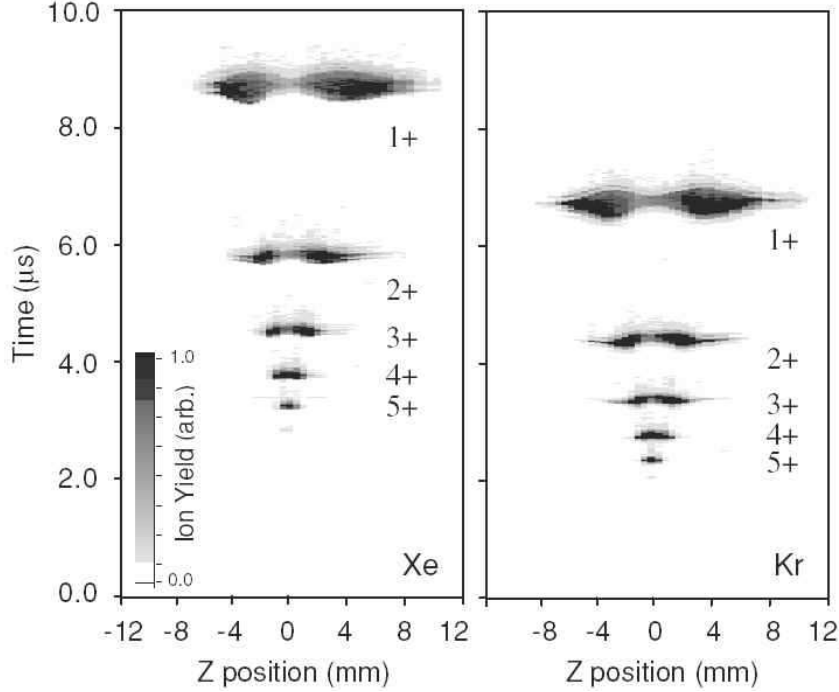


**Figure 1.** Z-scan time-of-flight matrices for Xe and Kr targets. Centrally located on each figure, the  $z = 0$  axis corresponds to the position of the peak laser intensity  $I_0$ . Ion yield profiles are generated by temporal integration of these plots.

the z-scan technique would yield complete intensity-dependent ionization curves for all observed charge states, and also allow a range of laser intensities to be investigated simultaneously. In light of this, we present a technique for the quantisation of the confocal volume to the order  $(\Delta z)^2$  using a parallel-projection inversion algorithm in conjunction with the z-scan technique.

## 2. Inversion Methodology

Inversion techniques allow determination of an object's internal properties through the deconvolution of a set of line integrals intersecting the object, perhaps the most familiar example of which is computer-assisted tomography (CAT) [10]. Generally, where the structure of the object is unknown, line integrals from a number of locations around the object are necessary to obtain the reconstructed image via an inversion technique such as the Radon transform [11]. However, if the structure of the object is known, or has rotational symmetry about an axis normal to the line integrals, the object may be reconstructed from observations at a single orbital location. In this instance, the object is the laser confocal volume, with the line integrals determined by integration of the rare gas target experimental z-scans which are shown in figure 1.

In this case, each of the  $n$  z-axial measurements ( $\eta_n$ ) represents the total integrated ion yield from all ionization processes within the discrete intensity range  $I(z)$  to  $I(z + \Delta z)$  along the z-axis, and an unbound range of intensities in the radial plane.

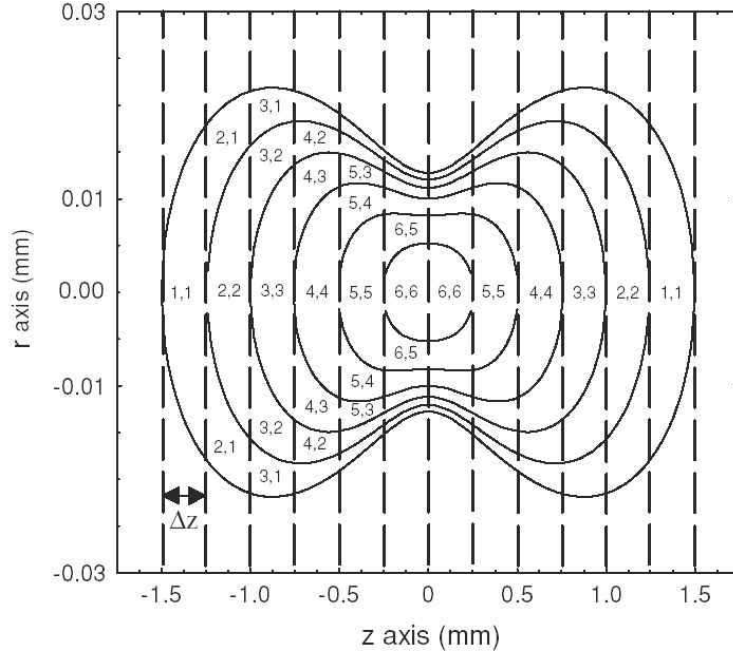


**Figure 2.** Quantisation of the confocal volume by z-scanning. The isointensity contours are given by equation 1, and the double indices throughout the figure refer to the volume elements  $V_{n,s}$ , where  $n$  denotes the slit position along the z-axis, and  $s$  denotes the isointensity contour.

By constructing a basis set of  $n$  Gaussian isointensity contours  $I_s$ , each separated by the imaging slit width  $\Delta z$  along the z-axis, the entire confocal volume can be quantised to the order  $(\Delta z)^2$  by known volume elements  $V_{n,s}$ , where  $n$  denotes the z-axial position and  $s$  refers to the isointensity contour. These quantised volume elements are aligned such that the boundary of each contour coincides with the edge of the imaging slit as shown in figure 2. Importantly, volume elements common to a particular isointensity shell will possess the same intensity  $I_s$  irrespective of the z-axial position ( $n$ ). The functional form of  $I_s$  is given in equation 1 where  $r$  is radial coordinate orthogonal to  $z$ , and  $\omega_o$  is the focused laser beam radius at the position  $z = 0$ .

$$I_s(z, r) = \frac{I_o}{1 + (z/z_o)^2} \exp\left(\frac{-2r^2}{(1 + (z/z_o)^2)\omega_o^2}\right) \quad (1)$$

Having fully quantised the confocal volume, the integrated ion yield profiles can be expressed through the simple matrix product  $\eta_n = V_{n,s} \xi_s$ , where  $\xi_s$  is the volume normalised, intensity-dependent ion yield. As the basis sets for  $n$  and  $s$  are coincident along the z-axis (see figure 2), the volume matrix is necessarily well-conditioned, and the system can be solved immediately for  $\xi_s$  by an inversion of the form:  $\xi_s = V_{n,s}^{-1} \eta_n$ .

The ion signal profiles used in the inversion algorithm were obtained from the experimental z-scans depicted in figure 1 by temporal (vertical axis) integration of the time-of-flight spectra for each  $z$ . This gave an ion signal intensity profile as a function of  $z$  for each observed ion species which in turn acted as the basis for

the inversion process. Diffraction effects present at very small  $z$  values, well above saturation intensities, act to form additional signal-producing volume over and above that expected through Gaussian volume calculations [8]. These additional volume elements were isolated and excluded from the reconstruction process. In any case the location of this effect, well above the saturation intensity, places it well out of the region of interest for the present study.

### 3. Experimental Configuration

The Wiley-McLaren type time-of-flight mass spectrometer used to collect the  $z$ -scan spectra has been described in detail elsewhere [12], hence only salient points will be discussed here. The confocal mask which enables  $z$ -scanning consists of a 0.5 mm diameter on-axis aperture situated at the top of a  $300 \text{ Vcm}^{-1}$  extraction region. For the current optical configuration, this can be approximated to a semi-infinite slit as the aperture diameter is much greater than the confocal waist for the full focal detuning range employed. The target gas is injected directly into the interaction region at a fill pressure of  $10^{-7}$  mbar on a background of  $10^{-10}$  mbar, well below the onset of any observable space-charge effects. At pressures greater than  $10^{-6}$  mbar space charge effects were observed as a widening of the ion peaks in the TOF spectra and as distortions in the  $z$ -scans. At pressures of  $10^{-7}$  mbar, these effects have disappeared. The gas is multiply ionized by 65 fs linearly polarised Ti:Sapphire laser pulses at 10 Hz repetition rate with a central wavelength of 790 nm, focused using  $f/34$  optics to a peak laser intensity of  $7 \times 10^{15} \text{ Wcm}^{-2}$ . The laser energy  $E$  ( $= 4 \text{ mJ}$ ) was measured using a calibrated power meter and the waist radius  $\omega_o$  ( $= 17 \mu\text{m}$ ) was calculated from  $\omega_o = 2f\lambda/\pi$  where  $f$  is the  $f$ -number ( $f = 34$ ) of the optical system. The peak intensity was calculated using  $I = E/\tau\pi\omega_o^2$ , where  $\tau$  is the laser pulse duration. The combination of errors associated with meter calibration and pulse duration measurement give an absolute error on the intensity of 30%, although the relative intensities are accurate to within 10%. The cylindrical symmetry of the focused beam is essentially preserved in the present optical configuration since the maximum angle of incidence of the laser beam is less than 0.5 degrees from the optical axis. This means transmission through the shallow focusing lens is essentially independent of the orientation of the polarisation vector with respect to the plane of incidence [13]. Ions produced during the laser interaction are detected by a microchannel plate detector outputting to a fast digital storage oscilloscope, where spectra are averaged over 500 shots. Shot to shot energy fluctuations were minimised by a discriminating photodiode. The focal lens was mounted on a computer controlled precision translation stage, allowing the focal detuning to be driven with a 0.25 mm step size with respect to the  $z$ -axis, permitting the production of 50-element  $z$ -scans. Figure 1 shows the raw  $z$ -scan spectra for xenon and krypton targets. Ions up to  $\text{Xe}^{5+}$  and  $\text{Kr}^{5+}$  were observed, and have been found to be in good agreement with other experiments employing rare gas targets at these intensities [4, 14].

### 4. Results and Discussion

It should be noted that the reconstruction method employed will yield ionization probability ( $P$ ) multiplied by the inherent quantum efficiency ( $q$ ) of the detector. Following application of the reconstruction algorithm, the derived Ionization Probability x Quantum Efficiency ( $q$ ) is mapped onto an intensity axis as shown in

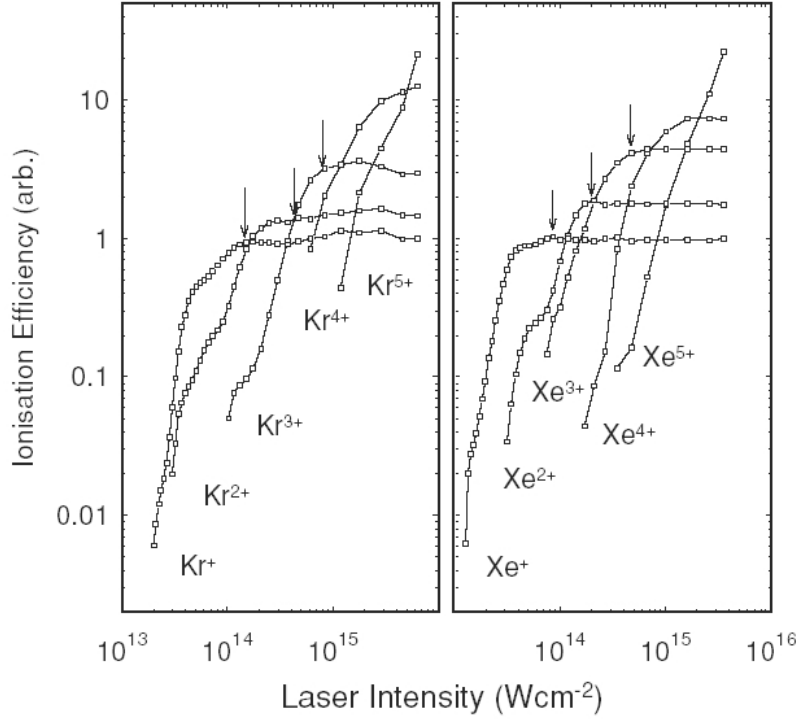


**Figure 3.** Reconstructed intensity-dependent, volume-normalised, Pq curves as a function of the discrete on-axis local peak intensity  $I_s$  for all observed charge states. The arrows indicate the saturation intensity expected under an ADK approximation.

figure 3. In doing so it is clear that the intensity-dependant Pq curves for each observed ion species are similar. Each curve is initiated at a threshold intensity  $I_{th}$ , followed by a rapid rise in the Pq characteristic of Stark-shifted multiphoton ionization. In turn, this is followed by a slow rate of increase, characteristic of tunnelling ionization until the Pq curve saturates. Considering the first ionization stage ( $Xe \rightarrow Xe^+$ ) as an example, it should be noted that the probability of observing  $Xe^+$  would actually decrease at intensities above saturation as multiple ionization becomes significant. However the probability of  $Xe^+$  being generated during the pulse is still  $Pq = 1$ , and since it provides a more informative insight into the field ionization dynamics, we have plotted this probability of production, as opposed to the probability of observation, in figure 3. The higher ionization stages display correspondingly higher values of Pq at which they saturate as a consequence of the varying quantum efficiency of the detector as a function of charge state. Indeed, measurement of the Pq values at saturation for multiply charged ions (figure 3) relative to the singularly charged ion Pq curve provides a direct experimental measure of the detector quantum efficiency. All Pq curves in figure 3 can therefore be normalized to a unit probability ( $P = 1$ ) at saturation. The Pq curves for the  $Xe^{4+}$  and  $Kr^{5+}$  are not saturated.

The Coulomb potential plus the laser electric field ( $\varepsilon$ ) gives rise to a total potential of  $V(r) = Zr^{-1} - \varepsilon \cdot r$ , where  $Z$  is the residual charge on the ion, and  $r$  is the radial distance from the charge centre. A saddle point in  $V(r)$  occurs for  $\varepsilon = \varepsilon_{sat} = Z^3 / (4n^*)^2$

[15], where  $n^*$  ( $= n - \delta_l$ ) is the effective principal quantum number, and  $\delta_l$  denotes the quantum defect [16]. The calculated  $\varepsilon_{sat}$  values, which are both charge and species specific, (shown by arrows in figure 3) are in excellent agreement with the present experimental saturation intensities. The tunnelling regions in figure 3, in particular for Kr+ and Xe+, display detail previously unseen in full confocal volume experiments. Indeed, this technique has, for the first time, allowed accurate determination of the gradient in this transitory regime to be made, which perhaps surprisingly displays an unexpected level of structure, including a species-specific gradient with Kr<sup>+</sup> having a slope three times that of Xe<sup>+</sup>. The explanation for this structure requires further investigation, but we may hypothesize as to the cause. This is the intensity region where rescattering of the ionised electron from the singly charged core has been shown to contribute to non-sequential double ionisation, probably via excitation followed by field ionisation [17]. It is quite likely that as well as ionisation, recombination, or indeed field-stimulated recombination is also occurring in the electron-ion interaction. This would have the effect of depleting the yield of singly charged ions, and hence could account for the observed structure.

Using perturbation theory, the low intensity Stark-shifted multiphoton region can be quantified by  $I^N \sigma$  where N is the number of photons and  $\sigma$  is the ionization cross-section. A  $\chi^2$  minimisation in this region yielded  $N = 6(8)$  for Xe, and  $N = 7(10)$  for Kr, less than the expected values shown in brackets, suggesting that the atomic potential is strongly influenced by dynamic Stark shifts of 3-5 eV or alternatively by transient population trapping [18].

The Xe<sup>2+</sup> and Kr<sup>2+</sup> Pq curves both display a characteristic knee structure separating the regions of non-sequential (NS) and sequential (S) ionization. The transition from NS to S ionization is completed by laser intensities of  $6 \times 10^{13}$  and  $8 \times 10^{13}$  Wcm<sup>-2</sup> in Xe<sup>2+</sup> and Kr<sup>2+</sup> respectively. The source of the NS signal below the knee has previously been attributed to a recollision mechanism [19]. At  $6 \times 10^{13}$  and  $8 \times 10^{13}$  Wcm<sup>-2</sup>, the corresponding maximum recollision energies are 12.9 and 16.6 eV, leaving a deficit of 8.3 and 7.8 eV against the ionization potentials of Xe<sup>+</sup> and Kr<sup>+</sup> respectively, indicative of excited states undergoing field or electron impact ionization. Recently, Becker and Faisal [20] have completed S-matrix calculations in which the primary ionized electron is dressed by the radiation field [21], which demonstrates the role of the laser field in electron impact ionization process. A more quantitative interpretation of the intensity-dependent Pq curves can be obtained by recasting the reconstructed curves in terms of the Keyldsh adiabaticity parameter  $\gamma$  [22], given in a convenient form by  $\gamma = (E_i/2U_P)^{1/2}$ , where  $E_i$  is the ionization potential of the target,  $\lambda$  is the wavelength in microns of the incident radiation field, and  $U_P$  is the ponderomotive or quiver energy of the electron in the field, calculated using  $U_P = 9.33 \times 10^{-14} \lambda^2 I$  (Wcm<sup>-2</sup>). As shown in figure 4, the curves for both Xe<sup>+</sup> and Kr<sup>+</sup> overlap well in  $\gamma$ -space, with saturated field ionization occurring for  $\gamma < 0.8$ , and the quantum mechanical tunnelling region straddling  $\gamma = 1$ , in excellent agreement with the theoretically predicted range of  $0.5 < \gamma < 1$  [15].

## 5. Conclusion

In conclusion, it has been shown that the use of a parallel-projection inversion algorithm has realised the full potential of the experimental z-scan technique by, for the first time, fully quantising the confocal interaction region, allowing production of volume normalised, intensity-dependent ion yield curves for a range of charge states

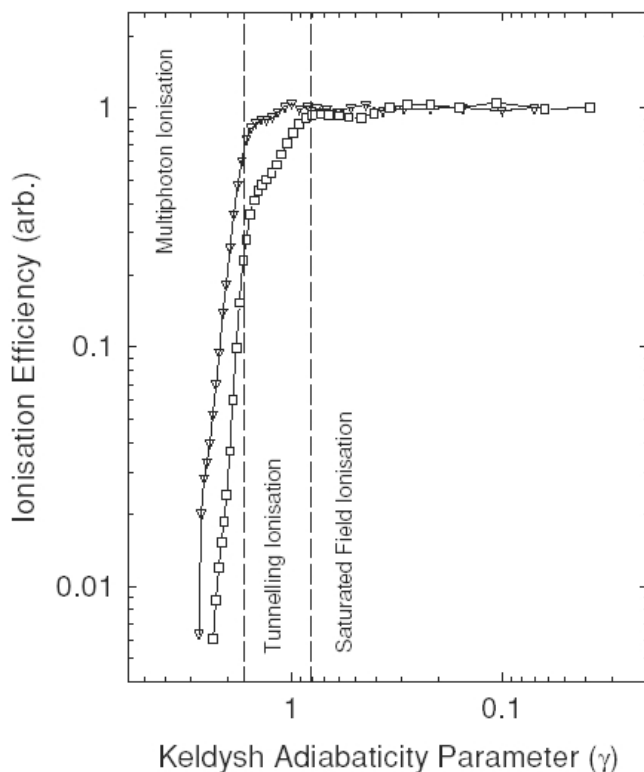


**Figure 4.** Intensity-dependent ionization probabilities for  $\text{Xe}^+$  ( $\nabla$ ) and  $\text{Kr}^+$  ( $\square$ ) as a function of the Keldysh parameter. The dashed lines divide the three key regions of atomic ionization.

in xenon and krypton.

The reported experiment is the first direct observation of intense-field atomic ionization efficiencies, independent of both radial intensity blurring and interaction volume effects, which would usually mask the subtle features detected in figure 3. With application to molecular targets, this novel technique will permit an insight into a wide range of intensity-dependent dissociation and ionization mechanisms with greater clarity.

### Acknowledgments

We wish to thank the staff of the ASTRA laser facility at the Rutherford Appleton Laboratory, A J Langley, C J Hooker and E J Divall for their expert assistance in the collection of experimental data. This work was supported by the Engineering and Physical Sciences Research Council. TRJG and WAB gratefully acknowledge EPSRC awards.

**References**

- [1] Agostini P et al, Phys. Rev. Lett. 42 (1979) 1127, Yamakawa K et al, Phys. Rev. Lett. 92 (2004) 123001, Rudenko A et al, Phys. Rev. Lett. 93 (2005) 253001
- [2] Laroche S, Talebpour A and Chin S L, J. Phys. B: At. Mol. Opt Phys. 31 (1998) 1201, and references therein.
- [3] L'Huillier et al, Atoms in Intense Laser Fields Ed. M Gavrila (Academic, New York) 1992
- [4] Augst S, Meyerhofer D D, Strickland D and Chin S L, J. Opt. Soc. Am. B 8 (1991) 858
- [5] Jones R R, Phys. Rev. Lett. 74 (1995) 1091
- [6] Hankin S M, Villeneuve D M, Corkum P B and Rayner D M, Phys. Rev. A. 64 (2001) 013405
- [7] Hansch P, Walker M A and Van Woerkom LD, Phys. Rev. A. 54 (1996) 2559
- [8] El-Zein A et al. Phys. Scripta T92 (2001) 119
- [9] Greenwood, J et al. Phys. Rev. Lett. 88 (2002) 233001
- [10] Herman G T, Image Reconstruction from Projections, Academic Press (1980)
- [11] Radon J, Math. Phys. 69 (1917) 262
- [12] Sanderson J H et al, Phys. Rev. A. 65 (2002) 043403
- [13] Ditchburn R W, Light, Blackie (1963)
- [14] Talebpour A et al, J. Phys. B: At. Mol. Opt. Phys. 30 (1997) 1721
- [15] Ilkov F A, Decker J E and Chin S L, J. Phys B: At. Mol. Opt. Phys. 25 (1992) 4005
- [16] Bethe H A and Salpeter E E, Quantum Mechanics of One and Two Electron Atoms, Springer (1957)
- [17] Feuerstein B et al, Phys. Rev. Lett. 87 (2001) 043003
- [18] Talebpour A, Chien C Y and Chin S L, J. Phys. B: At. Mol. Opt. Phys. 29 (1996) 5725
- [19] Corkum P B, Phys. Rev. Lett. 71 (1993) 1994
- [20] Becker A and Faisal F H M, J. Phys. B: At. Mol. Opt. Phys. 32 (1999) L335
- [21] Van der Hart H W, J. Phys. B: At. Mol. Opt. Phys. 34 (2001) L147
- [22] Keyldsh L V, J. Exp. Theor. Phys. 47 (1964) 1945